

New Descriptor for Glomerulus Detection in Kidney Microscopy Image

Tsuyoshi Kato^{†,‡,*}, Raissa Relator[†], Hayliang Ngouv[†],
Yoshihiro Hirohashi[†], Tetsuhiro Kakimoto[◇], Kinuya Okada[◇].

- [†] Faculty of Science and Engineering, Gunma University, Kiryu-shi, Gunma, 326–0338, Japan.
- [‡] Center for Informational Biology, Ochanomizu University, Bunkyo-ku, Tokyo, 112–8610, Japan.
- [◇] Research Division, Mitsubishi Tanabe Pharma Corporation, Toda-shi, Saitama, 376–8515, Japan.

Abstract

Background: Glomerulus detection is a key step in histopathological evaluation of microscopy images of kidneys. However, the task of automatic detection of glomeruli poses challenges due to the disparity in sizes and shapes of glomeruli in renal sections. Moreover, extensive variations of their intensities due to heterogeneity in immunohistochemistry staining are also encountered.

Despite being widely recognized as a powerful descriptor for general object detection, the rectangular histogram of oriented gradients (Rectangular HOG) suffers from many false positives due to the aforementioned difficulties in the context of glomerulus detection.

Results: A new descriptor referred to as Segmental HOG is developed to perform a comprehensive detection of hundreds of glomeruli in images of whole kidney sections. The new descriptor possesses flexible blocks that can be adaptively fitted to input images to acquire robustness to deformations of glomeruli. Moreover, the novel segmentation technique employed herewith generates high quality segmentation outputs and the algorithm is assured to converge to an optimal solution. Consequently, experiments using real world image data reveal that Segmental HOG achieves significant improvements in detection performance compared to Rectangular HOG.

Conclusion: The proposed descriptor and method for glomeruli detection present promising results and is expected to be useful in pathological evaluation.

1 Background

Renal glomeruli provide a filtration barrier that retains higher molecular weight proteins in blood circulation. In various renal diseases, damage of the glomerular filtration barrier can be observed as protein leakage into urine, known as proteinuria. Therefore, the pathological changes in renal glomeruli of animal disease models can provide important information in screening compounds that target such diseases.

Our goal is to perform high-throughput detection of glomeruli in huge microscopy images of animal disease models, whose sizes run up to the order of 10^8 pixels. While existing studies about automatic analysis of glomeruli in microscopy images of kidneys are present [23, 13], target images in these works are from human biopsy samples with relatively small sizes, and are not suitable for our purpose.

Compared to general object detection tasks, there are two particular obstacles in the case of glomerulus detection. The first obstacle arises from the non-rigid sizes and shapes of the targets within the images. Indeed, the sizes of glomeruli are stable *in vivo*, although they swell in unfavorable situations, e.g. hypertension [6] and diabetes [17], to some degree. Also, the sizes of glomeruli in a whole-kidney-section image could vary depending on which part of a glomerulus the cross section passes through. The shapes of the glomeruli are almost spherical, making the boundaries circular. To obtain the boundaries, one might try to fit an ellipse to each glomerulus. However, this approach yields large estimation errors because each glomerulus is deformed to some extent.

The second difficulty arising in glomerulus detection task is the high variation of the intensities. In histological evaluation, immunohistochemistry is usually used to demonstrate the distribution and location of proteins in sections. In our target images, sections are immunostained for desmin, a known glomerular injury marker. As a result, some glomeruli are stained, and some are not. Since many glomeruli are partly stained, yielding heterogeneously stained glomeruli, detection is more complicated. Furthermore, the stained tissues in the kidneys are not only from glomeruli but also from other tissues such as blood vessels.

To check the existence of a glomerulus at each location in a whole-kidney-section image, the sliding window technique [15, 14, 16, 20] is employed. Using this procedure, a frame goes over the input image to check at every possible location whether the target object exists, then, a descriptor of the sub-image is extracted.

Rectangular HOG (R-HOG) [4], a widely used and recognized efficient descriptor for object detection in the field of computer vision, is a potentially suitable candidate descriptor for glomeruli. It has the capacity to capture the information of the magnitudes of the gradients in the image. Therefore, it is robust to the change in intensities caused by the heterogeneity of the stained levels. Glomeruli are known to be composed of tightly packed cells, resulting to high gradients in images. Thus, a natural approach would be to use the magnitudes of these gradients as features for the glomeruli. While we have also previously attempted to directly exploit this attribute, we have found the detection performance to be poor, resulting to many false positives and low recall. In addition to the magnitudes of gradients, their directions are also important to distinguish glomeruli from the other tissues. Using R-HOG descriptors obtained from both the magnitudes and the directions of the gradients, glomeruli detection performance results to recall values high enough to be useful for pathological evaluation. However, it appeared that R-HOG still suffers from a considerable amount of false positives [5, 9, 8].

The high number of false positives from the previous studies [5, 9, 8] can be ascribed to the condition that the standard HOG such as the R-HOG has a rigid block division. Due to this rigidity, there are instances when a block is inside the glomerular area, and outside on another. Thus, extracted features from each block contain large variances, and robustness to the deformations of glomeruli is lost. Although there are several other known local descriptors such as scale-invariant feature transform (SIFT) image features [12], Haar-like features [20], and local binary patterns (LBP) [1], these do not possess a solution to be robust to the deformation of glomeruli for similar reasons.

In this study, we introduce a flexible block division to the HOG descriptor to improve the detection performance and reduce the number of false positives. A new feature, which we refer to as the Segmental HOG (S-HOG) descriptor, is proposed for glomerulus detection. The block division of S-HOG is based on the estimated boundary of the glomerulus that is obtained via a segmentation algorithm, which is also developed in this work. This renders the division of blocks to be more adaptable than the rigid block division of R-HOG, and allows feature vectors to clearly differentiate between the inside and the outside of the glomerulus. Moreover, since blocks are always within the glomerular area, gradient information in the same block between two glomeruli is expected to be more similar. Experiments conducted reveal that the number of false positives was halved, keeping almost all true positives when using S-HOG compared to the R-HOG.

Related Works

Segmentation is an important step to extract the S-HOG descriptors. Recent works on segmentation of glomeruli has been sparse [23, 13]. Nevertheless, there has been some research regarding segmentation of specific organs in general biomedical images, including region growing [7], level set method [3], and active contour model [10, 21, 22]. Majority of them are semi-automatic and require users' intervention, possess no guarantee of optimality [10, 21, 22], and are highly dependent on the initial solution provided by users as input. On the other hand, the segmentation algorithm developed in this study is ensured theoretically to obtain the optimal solution, producing high quality segmentation. In addition to the above-mentioned, most recent attempts include using deep learning [2]. Deep learning typically requires great computational and time resources, whereas the proposed algorithm can work even on a standard personal computer or a laptop.

The algorithm developed by Kvarnström et al. [11] is relevant to the proposed segmentation technique. Their algorithm for cell contour recognition is based on a dynamic program, where they first estimated the cell centers and constructed a ray from the center to each of m directions, where $m = 32$. Then they computed the boundary likeliness at n points on each ray, where they set $n = 30$. Their algorithm finds a smooth contour by taking a point on each ray to connect them. To get a closed contour, they presented two algorithms. The first algorithm poses n sub-problems where in each sub-problem, the initial point and the endpoint are the same. We shall refer to this algorithm here as the *exhaustive dynamic program* (EDP). Their second algorithm is a heuristic method that is faster than the first scheme, but possesses no guarantee for global optimality. In this study, we developed a new segmentation algorithm which we will refer to as *divide & conquer dynamic program* (DCDP). Compared to Kvarnström et al's algorithms [11], the advantages of the DCDP algorithm are as follows:

- DCDP is much faster than EDP, yet an exact optimal solution is always obtained.
- The boundary likeliness function is trained with a machine learning technique to precisely estimate boundaries of glomeruli.

2 Methods

In the proposed method, a new descriptor, S-HOG, is introduced to detect glomeruli in kidney microscopic images. Segmentation of glomeruli is needed to extract the S-HOG descriptor. For fast exhaustive detection of glomeruli from large microscopic images, pre-screening is performed with R-HOG which does not require prior segmentation. The proposed method consists of the three stages (Figure 1):

- pre-screening stage,
- segmentation stage, and
- classification stage.

In each stage, a support vector machine (SVM) [18, 19] is used with a different type of HOG descriptor, resulting in three SVMs in total. To obtain the S-HOG descriptor, we perform segmentation of glomeruli from the sub-images that passed the pre-screening (Figure 1). Hereinafter, we present the details of each stage, and discuss how training datasets for each SVM are constructed and the materials used in the experiments at the end of this section.

Pre-Screening

In the pre-screening stage, candidate glomeruli are detected from a kidney microscopy image using the sliding window technique. The window size is set to 200×200 in our experiments. R-HOG features, which are 512-dimensional vectors based on our selected parameter values, are extracted and judged by SVM, and non-maximal suppression is then performed to obtain candidate glomeruli.

Segmentation

Segmentation of glomeruli is performed on sub-images that passed the pre-screening. In the segmentation algorithm, the boundary of a glomerulus is represented by an m -sided polygon whose m vertices are restricted to lie on m line segments, respectively. The m line segments are placed uniformly, as outlined by the dotted lines in Figure 2b for the case where $m = 36$. To determine the location of the vertex on each line segment, the sliding window technique is employed again.¹ The window sweeps through the line segment and computes the *boundary likeliness* at n locations on the line segments. In Figure 2b, the boundary likeliness L_i ($i = 1, \dots, m$) is computed at every dotted location. How L_i is computed is discussed at the end of this **Segmentation** subsection. We set the length of the line segment to 63 pixels, where the endpoint closest to the center of the image is 17 pixels away from the center. The length between adjacent dots along a line segment is equal to 3 pixels, resulting to $n = 22$ dots on each line segment. In total, the boundary likeliness is computed at $mn (= 36 \times 22 = 792)$ locations. To determine the vertices of the m -sided polygon, one might consider naïvely locating the points that achieve the highest boundary likeliness on each line segment. However, this approach often yields an extremely zigzag boundary.

To obtain a smoother boundary, we impose a constraint that suppresses distant adjacent vertices. We then establish the following maximization problem:

$$\begin{aligned} \max \quad & \sum_{i=1}^m L_i(p_i), \quad \text{wrt } p_1, \dots, p_m \in \{1, \dots, n\}, \\ \text{subj to} \quad & |p_1 - p_2| \leq \varsigma, \dots, |p_{m-1} - p_m| \leq \varsigma, |p_m - p_1| \leq \varsigma, \end{aligned} \quad (1)$$

where $L_i : \{1, \dots, n\} \rightarrow \mathbb{R}$ denotes the boundary likeliness function obtained by the sliding window technique, and $p_i \in \{1, \dots, n\}$ ($i = 1, \dots, m$) is a location on the i -th line segment, where the line segment is discretized into n points numbered with a natural number. For instance, when $p_i = 1$, the i -th vertex is at the endpoint of the i -th line segment closest to the center, and the vertex can move from this endpoint to the other endpoint with increasing value of p_i . $L_i(p)$ is the boundary likeliness at p -th location in the i -th line segment. The location p_i on the i -th line segment is more likely to be the boundary with larger $L_i(p_i)$ value. In our experiments, we set $\varsigma = 1$. We shall denote the objective function by $J(\mathbf{p})$, i.e., $J(\mathbf{p}) := \sum_{i=1}^m L_i(p_i)$.

Kvarnström et al. tackled a similar optimization problem, and proposed an algorithm which we called EDP. In this study, a faster algorithm named DCDP is developed. The two algorithms, EDP and DCDP, are detailed as follows.

Exhaustive Dynamic Program (EDP). Due to the last constraint $|p_m - p_1| \leq \varsigma$, the standard dynamic program cannot directly solve optimization problem (1). To make the problem tractable, EDP divides problem (1) into n sub-problems, where the value of p_m is fixed to one of $\{1, \dots, n\}$ in each sub-problem. Once all the n sub-problems are solved, the optimal solution of the original problem (1) is obtained by taking the solution that yields the largest objective value among n sub-problems. Each sub-problem can be solved by a dynamic program that takes $O(nm\varsigma)$ computation. This algorithm computes an optimal solution of the k -th sub-problem, which is equivalent to the original problem (1) to which the constraint $p_m = k$ is added. Hence, the maximization problem (1) can be solved with $O(n^2m\varsigma)$ computation.

The new algorithm DCDP also takes $O(n^2m\varsigma)$ computational time in worst case, although the new algorithm solves the same problem much faster than EDP, as presented in the Results section.

¹Sliding windows are used in both pre-screening and segmentation.

Divide & Conquer Dynamic Program (DCDP). Observe that problem (1) can be solved in $O(nm\varsigma)$ computational time by a dynamic program if one of the constraints $|p_m - p_1| \leq \varsigma$ is disregarded. The idea to devise the new algorithm is based on the following fact: Suppose \mathbf{p}_0^* is an optimal solution that maximizes $J(\cdot)$ without the constraint $|p_m - p_1| \leq \varsigma$. Then if \mathbf{p}_0^* is a feasible solution for the original problem (1), it is also an optimal solution.

To express this idea mathematically, let us define

$$\mathcal{S}(\mathcal{I}) := \{ \mathbf{p} = (p_1, \dots, p_m) \in \mathbb{N}_n^m \mid \\ p_m \in \mathcal{I}, |p_1 - p_2| \leq \varsigma, \dots, |p_{m-1} - p_m| \leq \varsigma, |p_m - p_1| \leq \varsigma \}.$$

for $\mathcal{I} \subseteq \mathbb{N}_n$, where $\mathbb{N}_n := \{1, \dots, n\}$. Note that $\mathcal{S}(\mathbb{N}_n)$ is the feasible region of the original problem (1). The goal of DCDP is to find an optimal solution

$$\mathbf{p}^* \in \operatorname{argmax}_{\mathbf{p} \in \mathcal{S}(\mathbb{N}_n)} J(\mathbf{p}).$$

Dynamic program (DP) cannot solve this problem directly due to the existence of the constraint $|p_m - p_1| \leq \varsigma$. To use DP, we consider finding the maximizer of $J(\mathbf{p})$ from a relaxed region $\mathcal{S}_L(\mathbb{N}_n)$ where $\mathcal{S}_L(\mathcal{I})$ is defined as

$$\mathcal{S}_L(\mathcal{I}) := \{ \mathbf{p} = (p_1, \dots, p_m) \in \mathbb{N}_n^m \mid \\ p_m \in \mathcal{I}, p_1 \in \mathcal{I} + \{-\varsigma, \dots, +\varsigma\}, |p_1 - p_2| \leq \varsigma, \dots, |p_{m-1} - p_m| \leq \varsigma \},$$

where the operator $+$ denotes that for any two sets \mathcal{I} and \mathcal{J} , $\mathcal{I} + \mathcal{J} := \{i + j \mid i \in \mathcal{I}, j \in \mathcal{J}\}$. Note that $\mathcal{S}(\mathcal{I}) \subseteq \mathcal{S}_L(\mathcal{I})$. The strategy of DCDP is to first find the solution of the relaxed problem,

$$\mathbf{p}_0^* \in \operatorname{argmax}_{\mathbf{p} \in \mathcal{S}_L(\mathbb{N}_n)} J(\mathbf{p})$$

and then check the feasibility: if $\mathbf{p}_0^* \in \mathcal{S}(\mathbb{N}_n)$, then \mathbf{p}_0^* is the optimal solution of the original problem (1). If $\mathbf{p}_0^* \notin \mathcal{S}(\mathbb{N}_n)$, then the set \mathbb{N}_n is divided into \mathcal{I}_1 and \mathcal{I}_2 (i.e. $\mathcal{I}_1 \cup \mathcal{I}_2 = \mathbb{N}_n$), and the following two sub-problems are solved:

$$\mathbf{p}_1^* \in \operatorname{argmax}_{\mathbf{p} \in \mathcal{S}(\mathcal{I}_1)} J(\mathbf{p}) \quad \text{and} \quad \mathbf{p}_2^* \in \operatorname{argmax}_{\mathbf{p} \in \mathcal{S}(\mathcal{I}_2)} J(\mathbf{p}).$$

Notice that the original feasible region $\mathcal{S}(\mathbb{N}_n)$ is the sum of the two regions, $\mathcal{S}(\mathcal{I}_1)$ and $\mathcal{S}(\mathcal{I}_2)$. Therefore, we can take either of the two solutions, \mathbf{p}_1^* and \mathbf{p}_2^* , which has the larger objective value. DCDP employs a divide and conquer approach that repeatedly applies the above strategy to sub-problems. The basic approach of DCDP is summarized in Algorithm 1. Invoking the function `DCDP_BASIC`(\mathbb{N}_n) yields the optimal solution of the original problem. Here, the function $(\mathcal{I}_1, \mathcal{I}_2) := \text{SPLIT}(\mathcal{I}_0)$ divides the set \mathcal{I}_0 into two exclusive non-empty subsets, \mathcal{I}_1 and \mathcal{I}_2 .

Algorithm 1 $\mathbf{p}_0 = \text{DCDP_BASIC}(\mathcal{I}_0)$.

Input: $\mathcal{I}_0 \subseteq \mathbb{N}_n$.

Output: $\mathbf{p}_0 \in \operatorname{argmax}_{\mathbf{p} \in \mathcal{S}(\mathcal{I}_0)} J(\mathbf{p})$.

- 1: $\mathbf{p}_0 \in \operatorname{argmax}_{\mathbf{p} \in \mathcal{S}_L(\mathcal{I}_0)} J(\mathbf{p})$;
 - 2: **if** $\mathbf{p}_0 \in \mathcal{S}(\mathcal{I}_0)$, **then return**;
 - 3: $(\mathcal{I}_1, \mathcal{I}_2) := \text{SPLIT}(\mathcal{I}_0)$;
 - 4: $\mathbf{p}_1 := \text{DCDP_BASIC}(\mathcal{I}_1)$;
 - 5: $\mathbf{p}_2 := \text{DCDP_BASIC}(\mathcal{I}_2)$;
 - 6: $i^* \in \operatorname{argmax}_{i \in \{1, 2\}} J(\mathbf{p}_i)$;
 - 7: $\mathbf{p}_0 := \mathbf{p}_{i^*}$;
-

The first step $\mathbf{p}_0 \in \operatorname{argmax}_{\mathbf{p} \in \mathcal{S}_L(\mathcal{I}_0)} J(\mathbf{p})$ can be performed in $O(nm\varsigma)$ computational time. An instance of the dynamic program is given in Algorithm 2. Note that $\mathbf{p}_0 \in \mathcal{S}(\mathcal{I}_0)$ is always ensured if the cardinality of \mathcal{I}_0 is one since the relaxed region is reduced to the unrelaxed region (i.e. $\mathcal{S}(\{h\}) = \mathcal{S}_L(\{h\})$). The function `DCDP_BASIC` is invoked, at most, $(2n - 1)$ times. This implies that the computational time in worst case is $O(n^2m\varsigma)$. As will be shown in the Results section, we empirically found that the number of invoking the function recursively is much smaller than $(2n - 1)$.

To accelerate the DCDP algorithm, pruning steps are added. For the implementation of `SPLIT`(\mathcal{I}_0), we considered three schemes: *Half Split*, *Max Split*, and *Adap Split*. The pruning steps and the three schemes of `SPLIT`(\mathcal{I}_0) are detailed in Sections A and B, as well as the resulting accelerated DCDP algorithm. A mathematical proof using case analysis showing that our algorithm always obtains an optimal solution is also given in Section C.

Algorithm 2 $O(nm\varsigma)$ Dynamic Program for $\max_{\mathbf{p}^* \in \mathcal{S}_L(\mathcal{I})} J(\mathbf{p})$

Input: $\mathcal{I} \subseteq \mathbb{N}_n$.**Output:** $\mathbf{p} \in \operatorname{argmax}_{\mathbf{p} \in \mathcal{S}_L(\mathcal{I})} J(\mathbf{p})$

```
1: Initialize all entries in the  $n \times m$  matrix  $Q$  with  $-\infty$ .
2: for  $j \in \mathcal{I} + [-\varsigma, +\varsigma] \cap \mathbb{N}_n$  do
3:    $Q(j, 1) := L_1(j)$ ;
4: end for
5: for  $t = 2, \dots, m$  do
6:   if  $t < m$ , then  $\mathcal{I}_t := \mathbb{N}_n$  else  $\mathcal{I}_t := \mathcal{I}$ ;
7:   for  $i \in \mathcal{I}_t$  do
8:      $j_* := \operatorname{argmax}\{Q(j, t-1) \mid j \in [i-\varsigma, i+\varsigma] \cap \mathbb{N}_n\}$ ;
9:      $Q(i, t) := L_t(i) + Q(j_*, t-1)$ ;  $P(i, t) := j_*$ ;
10:  end for
11: end for
12:  $p_m^* \in \operatorname{argmax}_{i \in \mathcal{I}} Q(i, m)$ ;
13:  $t := m - 1$ ;
14: while  $t \geq 1$  do
15:    $p_t^* := P(p_{t+1}^*, t + 1)$ ;  $t := t - 1$ ;
16: end while
```

Computation of Boundary Likelihood $L_i(\cdot)$. The sliding window technique is employed in order to determine the vertices of the m -sided polygon described above. The window size in this stage is set to 30×15 pixels, and the windows sweep through the line segments (Figure 2b). Each time the sliding window moves, a feature descriptor is computed from the window and is applied with Linear SVM to compute the SVM score, which is what we refer to as the boundary likelihood $L_i(\cdot)$. The SVM scores of m vertices, $L_i(1), \dots, L_i(n)$, are then obtained for $i = 1, \dots, m$, and integrated in the maximization problem (1).

The HOG feature is adopted as the descriptor to compute the boundary likelihood. Each window is divided into three blocks as shown in Figure 2b. This division design is from an observation that some glomeruli are surrounded with a thick Bowman’s capsule, and the middle block is expected to capture this glomerular capsule. The statistics of nine discretely oriented gradients are computed in each block, producing a 27-dimensional feature vector.

Classification with S-HOG descriptor

Candidate glomeruli obtained via pre-screening are classified using the proposed S-HOG descriptor. S-HOG exploits the glomerulus boundary located in the segmentation stage to generate 24 non-overlapping blocks, as shown in Figure 3c.

Various types of glomeruli are contained in kidney microscopy images, some of them surrounded with a thick Bowman’s capsule. To effectively exploit this characteristic, the circle containing a candidate glomerulus is divided into three zones: Inner zone, middle zone, and outer zone. We divide the circle into eight disjoint sectors, and take the intersection of each zone and each sector to get the 24 non-overlapping blocks (Figure 3c), and gradients are then histogrammed for each block (Figure 3d). In our experiments, we employed nine discretized oriented gradients, and SVM is applied to S-HOG feature vectors to discriminate between glomeruli and non-glomeruli.

Construction of Training Data

A total of three linear SVMs are used, one for the pre-screening, segmentation, and classification stage, respectively. A training dataset is required for each of the three SVMs. Details on the construction of each training data set are given subsequently.

Training Data for Pre-Screening Stage. Each example in the training data for pre-screening is a 200×200 sub-image. A positive example contains a glomerulus in the center of the sub-image, while a negative example does not. To gather these samples, the locations of glomeruli within the whole-kidney-section images used for training are first annotated manually. Small glomeruli whose diameters are under 50 pixels were ignored. Positive examples are the sub-images from 200×200 bounding boxes containing an annotated glomerulus in the center. Negative examples are 200×200 sub-images picked from random locations in the kidney microscopy images. From each sample, a 512-dimensional R-HOG descriptor is extracted.

Training Data for Segmentation Stage. As described in the Segmentation subsection, the boundary likeliness is computed in every position on the m line segments. This boundary likeliness is the SVM score. The position lying on the true boundary of a glomerulus is considered as a positive example for the SVM, and the other positions are negative examples. To construct the training data for segmentation, the positive sub-images in the training dataset for pre-screening are reused.

Training Data for Classification Stage. Examples in the training data for pre-screening are used again for training in the classification stage, but with a different set of features extracted via S-HOG. For each training data sample, the previously described segmentation algorithm estimates the boundary of the glomerulus. Based on the estimated boundary, the statistics of oriented gradients are computed to obtain S-HOG feature vectors. This procedure is done for both positive and negative examples, even though negative examples do not contain a glomerulus.

Materials

The images used in the present study had been generated in a previous study [5], and only an overview is given in this subsection.

Male 6-week-old SD and SDT rats were purchased from CLEA, Inc. (Tokyo, Japan) and were housed with a 12-h light-dark cycle and free access to water and chow.

Five SD and SDT Rats at 16 and 24 weeks of age were euthanized under ether anesthesia. Their kidneys were removed and immediately fixed in 10% neutralized buffered formalin. The formalin-fixed kidneys were embedded in paraffin. For immunohistochemistry, kidney paraffin sections were deparaffinized and incubated overnight at 4°C with anti-desmin mouse monoclonal antibody (Dako, Glostrup, Denmark) followed by horseradish peroxidase-conjugated secondary antibody (anti-mouse immunoglobulin goat polyclonal antibody; Nichirei, Tokyo, Japan). The sections were colored brown with 3,3'-diaminobenzidine. Whole slide images of the sections were obtained with Aperio Scan Scope XT (Leica Microsystems, Wetzlar, Germany). All animal experiments were performed in accordance with the Act on Welfare and Management of Animals and the institutional guidelines, and approved by the institutional Committee of Animal Experiments of New Drug Development Research Center Inc. (Hokkaido, Japan).

3 Results and Discussion

In this section, the detection performance is demonstrated by showing the experimental comparisons between S-HOG and R-HOG [5, 9].

A set of 20 whole-kidney-section images is used in the experiments. The dataset is the same as the one used by [5]. The image sizes are $9,849 \times 10,944$ pixels in average. Each image is from one of four groups: 16-week-age SD rat, 16-week-age SDT rat, 24-week-age SD rat, and 24-week-age SDT rat. Henceforth, for simplicity, we will refer to them as 16SD, 16SDT, 24SD, 24SDT, respectively, each group containing five images. For performance evaluation, we annotated every glomerulus in the images manually. We divided the image set into five subsets: Set A, Set B, Set C, Set D, and Set E. Each subset consists of a 16SD image, a 16SDT image, a 24SD image, and a 24SDT image. For assessment of detection performance, the position of every glomerulus in the images is annotated and, for evaluation of segmentation performance, the areas of glomeruli in Set A and Set B are located manually using a graphics software.

As described in the previous section, our method has three stages: pre-screening, segmentation, and classification. Each stage uses its own SVM trained with a hyper-parameter C . In the classification stage, a threshold θ is used to classify an example; if the SVM score is over the threshold θ , the example is predicted as positive, otherwise, negative. For the pre-screening and classification stages, Set A was used for training SVM, and Set B was exploited for determining the optimal combination of (C, θ) . Sets C, D, and E were for performance evaluation. SVM for the segmentation stage provides us with the boundary likelihood function. The regularization parameter C for the SVM is determined via the holdout method within Set A. Seventy percent of the glomeruli in Set A are randomly selected for training, and the rest is used for validation. The resulting parameter values were $(C, \theta) = (10, 2)$ for pre-screening, $C = 10$ for segmentation, and $(C, \theta) = (10, -1.5)$ for classification.

Detection Performance

Figure 4 illustrates examples of detected glomeruli. In the two images, the candidate glomeruli passed through pre-screening are depicted with rings that represent the boundaries estimated in the segmentation stage. The numbers printed above the rings are the scores produced by SVM in the classification stage. Candidate glomeruli with SVM scores below $\theta = -1.5$ are excluded from the final detection results. The excluded candidates are depicted with blue rings, and the remaining glomeruli with red rings. It can be observed that non-glomerulus areas are excluded effectively, whereas true glomeruli are estimated correctly.

For quantitative assessment of detection performance, true positives, false positives, and false negatives have to be defined. True positive glomeruli (TPG) are identified as correctly detected glomeruli, false positive glomeruli (FPG) are wrongly detected glomeruli, and false negative glomeruli (FNG) are the ones that could not be detected. From the definitions of TPG, FPG, and FNG, we can compute for the three widely used performance measures: F-measure, Precision, and Recall. Precision is the ratio of TPG to detected glomeruli (i.e. $TPG/(TPG + FPG)$), Recall is the ratio of TPG to true glomeruli (i.e. $TPG/(TPG + FNG)$), and F-measure is the harmonic mean of the Precision and the Recall.

Figure 5 shows the plots of the F-measure, Precision, and Recall for each testing image. S-HOG achieves an average of 0.866, 0.874, and 0.897 for F-measure, Precision, and Recall, respectively, whereas R-HOG obtained 0.838, 0.777, and 0.911, respectively. In applying detection methods to pathological evaluation, Precision is more important than Recall [9], and in this study, S-HOG achieved considerably higher Precision at a small sacrifice of Recall. Two-sample t-test is performed to assess the differences statistically. While no statistical difference of Recall can be detected (P-value is $3.47 \cdot 10^{-1}$), the differences among F-measure and Precision are significant (P-values is $1.34 \cdot 10^{-3}$ and $3.75 \cdot 10^{-5}$, respectively),

Segmentation Performance

One advantage of the proposed method is that the boundaries of the detected glomeruli can be obtained. These boundaries provide useful information for pathological evaluation [9]. Here we give a discussion of the performance of the segmentation algorithm. To quantify the accuracy of the estimated areas within the predicted boundaries, 993 annotated glomeruli in Set B were used. True positive area (TPA), false positive area (FPA), and false negative area (FNA) are defined as follows: TPA is the intersection of the true area and estimated area; FPA is the relative complement of the true area in the estimated area; FNA is the relative complement of the estimated area in the true area. For each glomerulus and its estimated area, F-measure, Precision, and Recall can be obtained by counting the pixels in the TPA, FPA, and FNA. The histograms of the F-measure, Precision, and Recall are plotted in Figure 6, where the frequency is normalized so that the integral is one. Among the glomeruli, 90.1% are estimated to have F-measure over 0.8, ensuring reliable assessment of medicinal effect for pharmaceutical development.

The computational time of the new segmentation algorithm, DCDP, is compared with that of EDP. Note that the two algorithms solve the same optimization problem, and it can be shown that both algorithms always find an exact optimal solution. DCDP and EDP are implemented in C++ language, and the runtimes are measured on a Linux machine with Intel(R) Core(TM) i7 CPU and 8Gb memory. First, the number of times when the $O(nm\zeta)$ DP routine was invoked, which we denote by n_{dp} , is counted using the annotated glomeruli in Set B. Figure 7a shows the box-plot of n_{dp} for all methods. While the value of n_{dp} for EDP is always n , the values for DCDP depend on the input images and the splitting schemes, Half Split, Max Split, and Adap Split (Section B). For 46.32% of glomeruli, the optimal solutions are found within the first DP routine (i.e. $n_{dp} = 1$). The medians of the n_{dp} 's when using Half Split, Max Split, and Adap Split are 5, 3, 3, respectively. In other words, the medians of the depths of the branching tree for each scheme, respectively, are 3, 2 and 2. The 75 percentiles of n_{dp} 's are 11, 7, 5, respectively. For no glomeruli glomeruli, n_{dp} of Adap Split is larger than n , whereas the number of glomeruli with $n_{dp} > n$ are 4 (0.40%) and 16 (1.61%) for Half Split and Max Split. This implies that Adap Split is the smartest heuristic among the three splitting schemes. As considered in Subsection B.1, Adap Split produces the same solution \mathbf{p}_L in the branches less frequently than the three other schemes. In Half Split and Max Split, the frequencies (# of glomeruli) for the cases that the solution \mathbf{p}_L in the top branch appears again in the second branches is 414 and 314, respectively. Those numbers are much larger than the frequency in Adap Split which is only 97. This explains why Adap Split is faster. The actual runtimes of each methods are depicted in Figure 7b, where the medians of the computational times are 0.0866, 0.0570, 0.0560, and 0.418 msec, respectively, for Half Split, Max Split, Adap Split and EDP. The 75 percentiles of the computational times are 0.171, 0.117, 0.0856, and 0.426 msec, respectively. Since these values are proportional to the n_{dp} 's, then the ratios among the runtimes are almost same as the ratios among the n_{dp} 's. These results conclude that the proposed algorithm DCDP achieves an exact optimal solution much more efficiently than the existing algorithm EDP solves the same problem, and Adap Scheme is the fastest splitting scheme.

4 Conclusions

In this paper, a new descriptor, Segmental HOG, was proposed for specific organ detection in microscopy images. The descriptor was based on the boundary of glomeruli to acquire robustness to variations of intensities, sizes, and shapes. A new segmentation algorithm, DCDP, was developed to locate the boundary of possible candidates of glomeruli. Empirical results show significant improvement compared to the state-of-the-art descriptor, Rectangular HOG, for the task of glomerulus detection in microscopy images. Moreover, experimental results reveal that DCDP is much faster than the existing segmentation algorithm EDP.

Several possible extensions of the proposed method can be considered. For instance, appropriate size of the sliding window should be chosen if the proposed method is applied to microscopic images with different resolutions. Also, while the boundary likeliness function is the same for any direction in the segmentation algorithm, different boundary likeliness functions can be used for detecting other organs that have orientation. As for the block division of the S-HOG descriptor, 24 blocks are used in this study as depicted in Figure 3c, but a different number of blocks with a different division can be used for another application. Future work includes exploring such extensions in other applications of Segmental HOG.

A Pruning

Pruning can accelerate the DCDP algorithm. Consider the case where the lower bound ℓ , such that

$$\max_{\mathbf{p} \in \mathcal{S}(\mathbb{N}_n)} J(\mathbf{p}) \geq \ell,$$

is known in advance when searching for the solution in $\mathcal{S}(\mathcal{I}_0)$. If $\ell > \max_{\mathbf{p} \in \mathcal{S}_L(\mathcal{I}_0)} J(\mathbf{p})$, then no optimal solution is in $\mathcal{S}(\mathcal{I}_0)$ since

$$\max_{\mathbf{p} \in \mathcal{S}(\mathbb{N}_n)} J(\mathbf{p}) \geq \ell > \max_{\mathbf{p} \in \mathcal{S}_L(\mathcal{I}_0)} J(\mathbf{p}) \geq \max_{\mathbf{p} \in \mathcal{S}(\mathcal{I}_0)} J(\mathbf{p}).$$

Based on this fact, the pruning step is added to obtain Algorithm A, and we have the following lemma.

Lemma 1. For any subset $\mathcal{I}_0 \subseteq \mathbb{N}_n$ and $\forall \ell \in \mathbb{R} \cup \{-\infty\}$, when the algorithm runs with $(\mathbf{p}_0, J_0, \ell_0) = \text{DCDP}(\mathcal{I}_0, \ell)$, the returned tuple $(\mathbf{p}_0, J_0, \ell_0)$ satisfies one of the following:

- **Case G:** If $\max_{\mathbf{p} \in \mathcal{S}(\mathcal{I}_0)} J(\mathbf{p}) \geq \ell$, then

$$\mathbf{p}_0 \in \operatorname{argmax}_{\mathbf{p} \in \mathcal{S}(\mathcal{I}_0)} J(\mathbf{p}), \quad \text{and} \quad J_0 = \ell_0 = J(\mathbf{p}_0) \geq \ell.$$

- **Case L:** If $\max_{\mathbf{p} \in \mathcal{S}(\mathcal{I}_0)} J(\mathbf{p}) < \ell$, then $J_0 < \ell_0 = \ell$.

Algorithm A $(\mathbf{p}_0, J_0, \ell_0) = \text{DCDP}(\mathcal{I}_0, \ell)$. Modification of DCDP_BASIC by adding pruning steps.

Input: $\mathcal{I}_0 \subseteq \mathbb{N}_n$.

```

1:  $\mathbf{p}_L \in \operatorname{argmax}_{\mathbf{p} \in \mathcal{S}_L(\mathcal{I}_0)} J(\mathbf{p})$ ;
2: if  $\ell > J(\mathbf{p}_L)$  then
3:   {Rule A}
4:    $J_0 := -\infty$ ;  $\ell_0 := \ell$ ;
5:   return;
6: end if
7: if  $\mathbf{p}_L \in \mathcal{S}(\mathcal{I}_0)$  then
8:   {Rule B}
9:    $\mathbf{p}_0 := \mathbf{p}_L$ ;  $J_0 := J(\mathbf{p}_L)$ ;  $\ell_0 := \max(\ell, J_0)$ ;
10:  return;
11: end if
12: {Rule C}
13:  $(\mathcal{I}_1, \mathcal{I}_2) := \text{SPLIT}(\mathcal{I}_0)$ ;
14:  $(\mathbf{p}_1, J_1, \ell_1) := \text{DCDP}(\mathcal{I}_1, \ell)$ ;
15:  $(\mathbf{p}_2, J_2, \ell_2) := \text{DCDP}(\mathcal{I}_2, \ell)$ ;
16:  $i^* \in \operatorname{argmax}_{i \in \{1, 2\}} J_i$ ;
17:  $\mathbf{p}_0 := \mathbf{p}_{i^*}$ ;  $J_0 := J(\mathbf{p}_{i^*})$ ;
18:  $\ell_0 := \max(\ell_2, J_0)$ ;

```

Section C gives the proof of the lemma. Finally, from Lemma 1, we can derive the following theorem which is an important theoretical result of this study.

Theorem 1. The optimal solution of the problem (1) is obtained by invoking $(\mathbf{p}^*, J^*, \ell^*) = \text{DCDP}(\mathbb{N}_n, -\infty)$.

B Splitting Schemes

For the implementation of $\text{SPLIT}(\mathcal{I}_0)$, we considered three schemes: *Half Split*, *Max Split*, and *Adap Split*.

Half Split. In this scheme, the subset of indices \mathcal{I}_0 is simply divided into the first half and the second half. The resulting \mathcal{I}_1 and \mathcal{I}_2 are sets of consecutive integers. For instance, this scheme divides $\mathcal{I}_0 = \{7, 8, 9, 10, 11, 12\}$ into $\mathcal{I}_1 = \{7, 8, 9\}$ and $\mathcal{I}_2 = \{10, 11, 12\}$. To increase the lower-bound ℓ defined earlier, a heuristic that swaps \mathcal{I}_1 with \mathcal{I}_2 if

$$\max_{h \in \mathcal{I}_1} L_m(h) < \max_{h \in \mathcal{I}_2} L_m(h)$$

is employed.

Max Split. Similar to Half Split, \mathcal{I}_1 and \mathcal{I}_2 generated by Max Split are sets of consecutive integers, although the splitting points are different. The splitting point of Half Split is the center of the interval \mathcal{I}_0 , whereas the splitting point of Max Split is given by $h_*(\mathcal{I}_0) := \operatorname{argmax}_{h \in \mathcal{I}_0} L_m(h)$. For example, if $h_*(\mathcal{I}_0) = 8$ for $\mathcal{I}_0 = \{7, 8, 9, 10, 11, 12\}$, this scheme outputs $\mathcal{I}_1 = \{7, 8\}$ and $\mathcal{I}_2 = \{9, 10, 11, 12\}$. In general, the resulting divisions are given by

$$\mathcal{I}_1 := \{h \in \mathcal{I}_0 \mid h \leq h_*(\mathcal{I}_0)\}, \quad \text{and} \quad \mathcal{I}_2 := \{h \in \mathcal{I}_0 \mid h > h_*(\mathcal{I}_0)\}.$$

If $\operatorname{card}(\mathcal{I}_2) = 0$, the entry $h_*(\mathcal{I}_0)$ is moved from \mathcal{I}_1 to \mathcal{I}_2 . A heuristic that swaps \mathcal{I}_1 with \mathcal{I}_2 if $\operatorname{card}(\mathcal{I}_1) > \operatorname{card}(\mathcal{I}_2)$ is applied.

Adap Split. Different from the above two schemes, Adap Scheme adaptively determines the splitting point using the current solution $\mathbf{p}_{L,0} := \operatorname{argmax}_{\mathbf{p} \in \mathcal{S}_L(\mathcal{I}_0)} J(\mathbf{p})$. Let us denote the first entry and the last entry in the vector $\mathbf{p}_{L,0}$ by p_1^0 and p_m^0 , respectively. The splitting point of Adap Scheme is given by the center between p_1^0 and p_m^0 . For instance, when $p_1^0 = 9$ and $p_m^0 = 12$ $\mathcal{I}_0 = \{7, 8, 9, 10, 11, 12\}$, this splitting scheme divides \mathcal{I}_0 into $\mathcal{I}_1 = \{7, 8, 9, 10\}$ and $\mathcal{I}_2 = \{11, 12\}$. In general, the resulting divisions are given by

$$\mathcal{I}_1 := \left\{ h \in \mathcal{I}_0 \mid h \leq \frac{p_1^0 + p_m^0}{2} \right\}, \quad \text{and} \quad \mathcal{I}_2 := \left\{ h \in \mathcal{I}_0 \mid h > \frac{p_1^0 + p_m^0}{2} \right\}.$$

The smallest entry in \mathcal{I}_2 is moved to \mathcal{I}_1 if $\operatorname{card}(\mathcal{I}_1) = 0$. The largest entry in \mathcal{I}_1 is moved to \mathcal{I}_2 if $\operatorname{card}(\mathcal{I}_2) = 0$. A swapping heuristic used in Max Split is then applied.

B.1 Why Adap Split is better

Adap Scheme is expected to be the smartest heuristic among the three splitting schemes. To describe the reason, let us illustrate the process of DCDP on a small toy problem with $(n, m, \varsigma) = (12, 8, 1)$ shown in Figure 8. The original problem and the relaxed problem are depicted in Figure 8a,b, respectively. When running $\operatorname{DCDP}(\mathbb{N}_8, -\infty)$, it is observed that $\mathbf{p}_{L,0} := \operatorname{argmax}_{\mathbf{p} \in \mathcal{S}_L(\mathcal{I}_0)} J(\mathbf{p}) \notin \mathcal{S}(\mathcal{I}_0)$, and thereby the set \mathcal{I}_0 is divided into \mathcal{I}_1 and \mathcal{I}_2 to produce two new branches $\operatorname{DCDP}(\mathcal{I}_1, -\infty)$ and $\operatorname{DCDP}(\mathcal{I}_2, \ell_1)$ where ℓ_1 will be computed by the former branch $\operatorname{DCDP}(\mathcal{I}_1, -\infty)$.

If using the Adap Split scheme, the two subsets are $\mathcal{I}_1 = \{7, 8\}$ and $\mathcal{I}_2 = \{1, 2, 3, 4, 5, 6\}$. In the branch of $\operatorname{DCDP}(\mathcal{I}_1, -\infty)$, $\mathbf{p}_{L,1} := \operatorname{argmax}_{\mathbf{p} \in \mathcal{S}_L(\mathcal{I}_1)} J(\mathbf{p})$ is in $\mathcal{S}(\mathcal{I}_1)$ (as shown in Figure 8c), implying that $\mathbf{p}_{L,1}$ is the maximizer of $J(\mathbf{p})$ over $\mathcal{S}(\mathcal{I}_1)$ and no more branching occurs. $\ell_1 = J(\mathbf{p}_{L,1}) = 10.1$ is set. Next, $\operatorname{DCDP}(\mathcal{I}_2, \ell_1)$ is invoked and $\mathbf{p}_{L,2} := \operatorname{argmax}_{\mathbf{p} \in \mathcal{S}_L(\mathcal{I}_2)} J(\mathbf{p})$ is computed in the branch (Figure 8d). It is then observed that $J(\mathbf{p}_{L,2}) = 9.5 < 10.1 = \ell_1$, which implies that the optimal solution is not in $\mathcal{S}(\mathcal{I}_2)$. Hence, $\mathbf{p}_{L,1}$ turns out the optimal solution of the original solution.

Meanwhile, if Half Split is applied, the set $\mathcal{I}_0 = \mathbb{N}_8$ is divided into $\mathcal{I}_1 = \{5, 6, 7, 8\}$ and $\mathcal{I}_2 = \{1, 2, 3, 4\}$ (Figure 8e,f). In the branch of $\operatorname{DCDP}(\mathcal{I}_1, -\infty)$, the solution of the relaxed problem is again $\mathbf{p}_{L,1} := \operatorname{argmax}_{\mathbf{p} \in \mathcal{S}_L(\mathcal{I}_1)} J(\mathbf{p}) = \mathbf{p}_{L,0} \notin \mathcal{S}(\mathcal{I}_1)$, leading to further branching of this branch (Figure 8e). Actually, in our experiments described in Results section, it is observed that Half Split and Max Split frequently encounter $\mathbf{p}_{L,1} = \mathbf{p}_{L,0}$ or $\mathbf{p}_{L,2} = \mathbf{p}_{L,0}$. Whenever $\mathbf{p}_{L,1} = \mathbf{p}_{L,0}$, further new branches for the divisions of \mathcal{I}_1 are produced, because $\mathbf{p}_{L,1} = \mathbf{p}_{L,0} \notin \mathcal{S}(\mathcal{I}_0)$ leading to $\mathbf{p}_{L,1} \notin \mathcal{S}(\mathcal{I}_1) \subset \mathcal{S}(\mathcal{I}_0)$. Similarly, when $\mathbf{p}_{L,2} = \mathbf{p}_{L,0}$, further new branches for the divisions of \mathcal{I}_1 are always born.

In Adap Split, as described in Results section, $\mathbf{p}_{L,1} = \mathbf{p}_{L,0}$ or $\mathbf{p}_{L,2} = \mathbf{p}_{L,0}$ is less likely to happen, resulting in less branches.

C Proof of Lemma 1

We shall use the following notation: For any $\mathcal{I} \subseteq \mathbb{N}_n$,

$$J(\mathcal{I}) := \max_{\mathbf{p} \in \mathcal{S}(\mathcal{I})} J(\mathbf{p}), \quad \text{and} \quad J_L(\mathcal{I}) := \max_{\mathbf{p} \in \mathcal{S}_L(\mathcal{I})} J(\mathbf{p}).$$

The following relationships will be used in this proof:

$$J(\mathbf{p}_L) \stackrel{(\text{eqA})}{=} J_L(\mathcal{I}_0) \stackrel{(\text{ineqA})}{\geq} J(\mathcal{I}_0) \stackrel{(\text{eqB})}{=} \max(J(\mathcal{I}_1), J(\mathcal{I}_2)),$$

where the labels (eqA), (ineqA), and (eqB) are used to distinguish these equalities and the inequality in later descriptions of this proof. The inequality follows from the fact that $\mathcal{S}(\mathcal{I}_0) \subseteq \mathcal{S}_L(\mathcal{I}_0)$, while the second equality eqB follows from $\mathcal{S}(\mathcal{I}_0) = \mathcal{S}(\mathcal{I}_1) \cup \mathcal{S}(\mathcal{I}_2)$.

We will prove the lemma by induction. For the case where $\text{card}(\mathcal{I}_0) = 1$, observe that $\mathcal{S}_L(\mathcal{I}_0) = \mathcal{S}(\mathcal{I}_0)$, implying that

$$\mathbf{p}_L \in \underset{\mathbf{p} \in \mathcal{S}(\mathcal{I}_0)}{\text{argmax}} J(\mathbf{p}) \quad \text{and} \quad J(\mathcal{I}_0) = J_L(\mathcal{I}_0) = J_0.$$

If $J(\mathcal{I}_0) = J(\mathbf{p}_L) < \ell$, then by Rule A in the algorithm, $J_0 = -\infty$ and $J_0 < \ell_0 = \ell$. On the other hand, if $J(\mathbf{p}_L) \geq \ell$, then since $\mathbf{p}_L \in \underset{\mathbf{p} \in \mathcal{S}(\mathcal{I}_0)}{\text{argmax}} J(\mathbf{p})$, we have $\mathbf{p}_L \in \mathcal{S}(\mathcal{I}_0)$. Thus, by Rule B, we have $\mathbf{p}_0 = \mathbf{p}_L$ and $J_0 = \ell_0 \geq \ell$. Therefore, the lemma is true for $\text{card}(\mathcal{I}_0) = 1$.

Let us now assume that the lemma holds for any $\mathcal{I}_0 \subseteq \mathbb{N}_n$ such that $\text{card}(\mathcal{I}_0) < k$ to show that the lemma is also established for any \mathcal{I}_0 such that $\text{card}(\mathcal{I}_0) = k$. Now suppose that $\mathcal{I}_0 \subseteq \mathbb{N}_n$ and $\text{card}(\mathcal{I}_0) = k$. The following is an exhaustive list of all possible cases:

- (1) $\ell > J_L(\mathcal{I}_0)$,
- (2) $J_L(\mathcal{I}_0) \geq \ell$ and $\mathbf{p}_L \in \mathcal{S}(\mathcal{I}_0)$,
- (3) $J_L(\mathcal{I}_0) \geq J(\mathcal{I}_0) = J(\mathcal{I}_1) = J(\mathcal{I}_2) \geq \ell$ and $\mathbf{p}_L \notin \mathcal{S}(\mathcal{I}_0)$,
- (4) $J_L(\mathcal{I}_0) \geq J(\mathcal{I}_0) = J(\mathcal{I}_1) \geq \ell > J(\mathcal{I}_2)$ and $\mathbf{p}_L \notin \mathcal{S}(\mathcal{I}_0)$,
- (5) $J_L(\mathcal{I}_0) \geq J(\mathcal{I}_0) = J(\mathcal{I}_1) > J(\mathcal{I}_2) \geq \ell$ and $\mathbf{p}_L \notin \mathcal{S}(\mathcal{I}_0)$,
- (6) $J_L(\mathcal{I}_0) \geq J(\mathcal{I}_0) = J(\mathcal{I}_2) > J(\mathcal{I}_1) \geq \ell$ and $\mathbf{p}_L \notin \mathcal{S}(\mathcal{I}_0)$,
- (7) $J_L(\mathcal{I}_0) \geq J(\mathcal{I}_0) = J(\mathcal{I}_2) \geq \ell > J(\mathcal{I}_1)$ and $\mathbf{p}_L \notin \mathcal{S}(\mathcal{I}_0)$,
- (8) $J_L(\mathcal{I}_0) \geq \ell > J(\mathcal{I}_0)$ and $\mathbf{p}_L \notin \mathcal{S}(\mathcal{I}_0)$.

We shall show that for each of the seven cases above, either Case G or Case L is true.

- (1) Since $\ell > J_L(\mathcal{I}_0) \stackrel{(\text{eqA})}{=} J(\mathbf{p}_L) \stackrel{(\text{ineqA})}{\geq} J(\mathcal{I}_0)$, then by Rule A, we have $J_0 = -\infty$ and $J_0 < \ell_0 = \ell$. Thus, Case L is satisfied.
- (2) If $J_L(\mathcal{I}_0) \geq \ell$, then $J(\mathbf{p}_L) \geq \ell$. Moreover, $\mathbf{p}_L \in \mathcal{S}(\mathcal{I}_0)$ implies $\mathbf{p}_L \in \underset{\mathbf{p} \in \mathcal{S}(\mathcal{I}_0)}{\text{argmax}} J(\mathbf{p})$ and $J(\mathbf{p}_L) = J(\mathcal{I}_0)$. Then by Rule B, $J_0 = J(\mathbf{p}_L) = J(\mathcal{I}_0) = \ell_0$ and $\mathbf{p}_0 = \mathbf{p}_L \in \underset{\mathbf{p} \in \mathcal{S}(\mathcal{I}_0)}{\text{argmax}} J(\mathbf{p})$. Therefore, Case G holds.
- (3) Given $J(\mathbf{p}_L) \stackrel{(\text{eqA})}{=} J_L(\mathcal{I}_0) \geq \ell$ and $\mathbf{p}_L \notin \mathcal{S}(\mathcal{I}_0)$, Rule C is applied. Observe that $(\mathbf{p}_1, J_1, \ell_1)$ satisfies Case G since $J(\mathcal{I}_1) = \max_{\mathbf{p} \in \mathcal{S}(\mathcal{I}_1)} J(\mathbf{p}) \geq \ell$. Thus, $J_1 = \ell_1 = J(\mathcal{I}_1) \geq \ell$. Similarly, $(\mathbf{p}_2, J_2, \ell_2)$ also satisfies Case G, and we have $J_2 = \ell_2 = J(\mathcal{I}_2) \stackrel{(\text{eqB})}{=} J(\mathcal{I}_1) = J(\mathcal{I}_0)$. Therefore, the returned value \mathbf{p}_0 of $\text{DCDP}(\mathcal{I}_0, \ell)$ is equal to \mathbf{p}_1 or to \mathbf{p}_2 , both of which are in $\underset{\mathbf{p} \in \mathcal{S}(\mathcal{I}_0)}{\text{argmax}} J(\mathbf{p})$. Furthermore, we obtain $\ell_0 = J_0 = J_1 = J_2 = J(\mathcal{I}_0) \geq \ell$. Hence, we have Case G.
- (4) As with Case (3), $(\mathbf{p}_1, J_1, \ell_1)$ satisfies Case G, and we have $\mathbf{p}_1 \in \underset{\mathbf{p} \in \mathcal{S}(\mathcal{I}_1)}{\text{argmax}} J(\mathbf{p})$ and $J_1 = \ell_1 = J(\mathcal{I}_1) \geq \ell$. An so it follows that $\max_{\mathbf{p} \in \mathcal{S}(\mathcal{I}_2)} J(\mathbf{p}_2) = J(\mathcal{I}_2) < \ell \leq \ell_1$, and Case L holds for $(\mathbf{p}_2, J_2, \ell_2)$ with $J_2 < \ell_2 = \ell_1$. Therefore, output $\mathbf{p}_0 = \mathbf{p}_1$, which is in $\underset{\mathbf{p} \in \mathcal{S}(\mathcal{I}_0)}{\text{argmax}} J(\mathbf{p})$ since $\mathcal{S}(\mathcal{I}_1) \subset \mathcal{S}(\mathcal{I}_0)$, and $J_0 = J_1 = \ell_2 = \ell_0 \geq \ell$. This gives us Case G.
- (5) In a similar logic as in Case (4), Case G is true for $(\mathbf{p}_1, J_1, \ell_1)$, and $\mathbf{p}_1 \in \underset{\mathbf{p} \in \mathcal{S}(\mathcal{I}_1)}{\text{argmax}} J(\mathbf{p})$ and $J_1 = \ell_1 = J(\mathcal{I}_1) \geq \ell$. Given that $J(\mathcal{I}_2) < J(\mathcal{I}_1)$, then $J(\mathcal{I}_2) < \ell_1$, hence, Case L also holds for $(\mathbf{p}_2, J_2, \ell_2)$ in this sub-case. Therefore, the same conclusion from Case (4) follows.
- (6) Since $\mathbf{p}_L \notin \mathcal{S}(\mathcal{I}_0)$, Rule C is implemented. Note that with $\max_{\mathbf{p} \in \mathcal{S}(\mathcal{I}_1)} J(\mathbf{p}) = J(\mathcal{I}_1) \geq \ell$, $(\mathbf{p}_1, J_1, \ell_1)$ follows Case G, and we have $J_1 = \ell_1 = J(\mathcal{I}_1) \geq \ell$. This implies that $J(\mathcal{I}_2) > J(\mathcal{I}_1) = \ell_1$. Therefore, Case G also holds for $(\mathbf{p}_2, J_2, \ell_2)$, and we obtain $J_2 = \ell_2 = J(\mathcal{I}_2) > J(\mathcal{I}_1) = J_1$. Thus, $\text{DCDP}(\mathcal{I}_0, \ell)$ outputs $\mathbf{p}_0 = \mathbf{p}_2 \in \underset{\mathbf{p} \in \mathcal{S}(\mathcal{I}_0)}{\text{argmax}} J(\mathbf{p})$ and $J_0 = J_2 = \ell_2 = \ell_0 > \ell$. Hence, Case G holds.

- (7) Similar to the previous cases, we apply Rule C. Given $\ell > J(\mathcal{I}_1) = \max_{\mathbf{p} \in \mathcal{S}(\mathcal{I}_1)} J(\mathbf{p})$, by Case L, $J_1 < \ell_1 = \ell$. and so it follows that $J(\mathcal{I}_2) \geq \ell_1 = \ell$. Therefore, $(\mathbf{p}_2, J_2, \ell_2)$ satisfies Case G, with $J_2 = \ell_2 = J(\mathcal{I}_2) > \ell$. Hence, the returned values of DCDP(\mathcal{I}_0, ℓ) are $\mathbf{p}_0 = \mathbf{p}_2 \in \operatorname{argmax}_{\mathbf{p} \in \mathcal{S}(\mathcal{I}_0)} J(\mathbf{p})$ and $J_0 = J_2 = \ell_2 = \ell_0 > \ell$, and Case G is satisfied.
- (8) Likewise, we implement Rule C for this case. Observe that since $\max(J(\mathcal{I}_1), J(\mathcal{I}_2)) \stackrel{(\text{eqB})}{=} J(\mathcal{I}_0) < \ell$, then both $(\mathbf{p}_1, J_1, \ell_1)$ and $(\mathbf{p}_2, J_2, \ell_2)$ satisfy Case L. Thus, we have $J_1 < \ell_1 = \ell$ and $J_2 < \ell_1 = \ell_2$. Therefore, DCDP(\mathcal{I}_0, ℓ) outputs $J_0 = \max(J_1, J_2) < \ell_2 = \ell_0 = \ell_1 = \ell$, which corresponds to Case L.

References

- [1] T. Ahonen, A. Hadid, and M. Pietikainen. Face description with local binary patterns: application to face recognition. *IEEE Trans Pattern Anal Mach Intell*, 28(12):2037–2041, Dec 2006.
- [2] Dan Cirosan, Alessandro Giusti, Luca M. Gambardella, and Jürgen Schmidhuber. Deep neural networks segment neuronal membranes in electron microscopy images. In F. Pereira, C.J.C. Burges, L. Bottou, and K.Q. Weinberger, editors, *NIPS*, pages 2852–2860, 2012.
- [3] Daniel Cremers, Mikael Rousson, and Rachid Deriche. A review of statistical approaches to level set segmentation: Integrating color, texture, motion and shape. *Int J Comput Vision*, 72(2):195–215, April 2007.
- [4] Navneet Dalal and Bill Triggs. Histograms of oriented gradients for human detection. In *IEEE CVPR*, volume 1, pages 886–893, Washington, DC, USA, 2005. IEEE Computer Society.
- [5] Yoshihiro Hirohashi, Raissa Relator, Tetsuhiro Kakimoto, Ryuta Saito, Yasushi Horai, Atsushi Fukunari, Hiroyuki Utsumi, Kinya Okada, and Tsuyoshi Kato. Automated quantitative image analysis of glomerular desmin immunostaining as a sensitive injury marker in spontaneously diabetic torii rats. *Journal of Biomedical Image Processing*, 1(1):20–28, May 2014.
- [6] M. D. Hughson, V. G. Puelles, W. E. Hoy, R. N. Douglas-Denton, S. A. Mott, and J. F. Bertram. Hypertension, glomerular hypertrophy and nephrosclerosis: the effect of race. *Nephrol Dial Transplant*, 29(7):1399–1409, Dec 2013.
- [7] H. Jiang, B. He, D. Fang, Z. Ma, B. Yang, and L. Zhang. A region growing vessel segmentation algorithm based on spectrum information. *Comput Math Methods Med*, 2013, 2013.
- [8] T. Kakimoto, K. Okada, K. Fujitaka, M. Nishio, T. Kato, A. Fukunari, and H. Utsumi. Quantitative analysis of markers of podocyte injury in the rat puromycin aminonucleoside nephropathy model. *Exp Toxicol Pathol*, 67(2):171–177, Feb 2015.
- [9] Tetsuhiro Kakimoto, Kinya Okada, Yoshihiro Hirohashi, Raissa Relator, Mizue Kawai, Taku Iguchi, Keisuke Fujitaka, Masashi Nishio, Tsuyoshi Kato, Atsushi Fukunari, and Hiroyuki Utsumi. Automated image analysis of a glomerular injury marker desmin in SDT rats treated with losartan. *Journal of Endocrinology*, 222(1):43–51, -2014.
- [10] Michael Kass, Andrew Witkin, and Demetri Terzopoulos. Snakes: Active contour models. *Int J Comput Vision*, 1(4):321–331, 1988.
- [11] Mats Kvarnström, Katarina Logg, Alfredo Diez, Kristofer Bodvard, and Mikael Käll. Image analysis algorithms for cell contour recognition in budding yeast. *Opt Express*, 16(17):12943–12957, Aug 2008.
- [12] David G Lowe. Distinctive image features from scale-invariant keypoints. *Int J Comput Vision*, 60(2):91–110, 2004.
- [13] Jiaxin Ma, Jun Zhang, and Jinglu Hu. Glomerulus extraction by using genetic algorithm for edge patching. In *IEEE CEC*, pages 2474–2479, Trondheim, Norway, 2009.
- [14] S. Maji, A. Berg, and J. Malik. Classification using intersection kernel support vector machines is efficient. In *IEEE CVPR*, pages 1–8, Anchorage, AK, June 2008.
- [15] S. Munder and D. M. Gavrilu. An experimental study on pedestrian classification. *IEEE Trans Pattern Anal Mach Intell*, 28(11):1863–1868, Nov 2006.
- [16] Constantine Papageorgiou and Tomaso Poggio. A trainable system for object detection. *Int J Comput Vision*, 38(1):15–33, 2000.

- [17] R. Rasch, F. Lauszus, J. S. Thomsen, and A. Flyvbjerg. Glomerular structural changes in pregnant, diabetic, and pregnant-diabetic rats. *APMIS*, 113(7-8):465–472, Jul-Aug 2005.
- [18] Bernhard Schölkopf and Alex J. Smola. *Learning with kernels*. MIT Press, Cambridge, MA, 2002.
- [19] John Shawe-Taylor and Nello Cristianini. *Kernel Methods for Pattern Analysis*. Cambridge University Press, Cambridge, MA, 2004.
- [20] Paul Viola and Michael J. Jones. Robust real-time face detection. *Int J Comput Vision*, 57(2):137–154, May 2004.
- [21] T. Wang, I. Cheng, and A. Basu. Fluid vector flow and applications in brain tumor segmentation. *IEEE Trans Biomed Eng*, 56(3):781–789, Mar 2009.
- [22] X. Xie. Active contouring based on gradient vector interaction and constrained level set diffusion. *IEEE Trans Image Process*, 19(1):154–164, Jan 2010.
- [23] Jun Zhang and Jinglu Hu. Glomerulus extraction by optimizing the fitting curve. In *ISCID*, volume 1, pages 169–172, 2008.

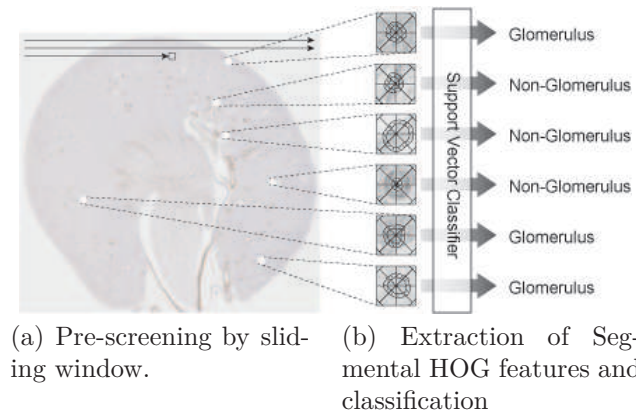


Figure 1: **Flow of Our Method.** In this study, a new descriptor, Segmental HOG, is developed to detect glomeruli in huge microscopy images. SVM is combined with Segmental HOG to classify candidates of glomeruli that passed the pre-screening stage.

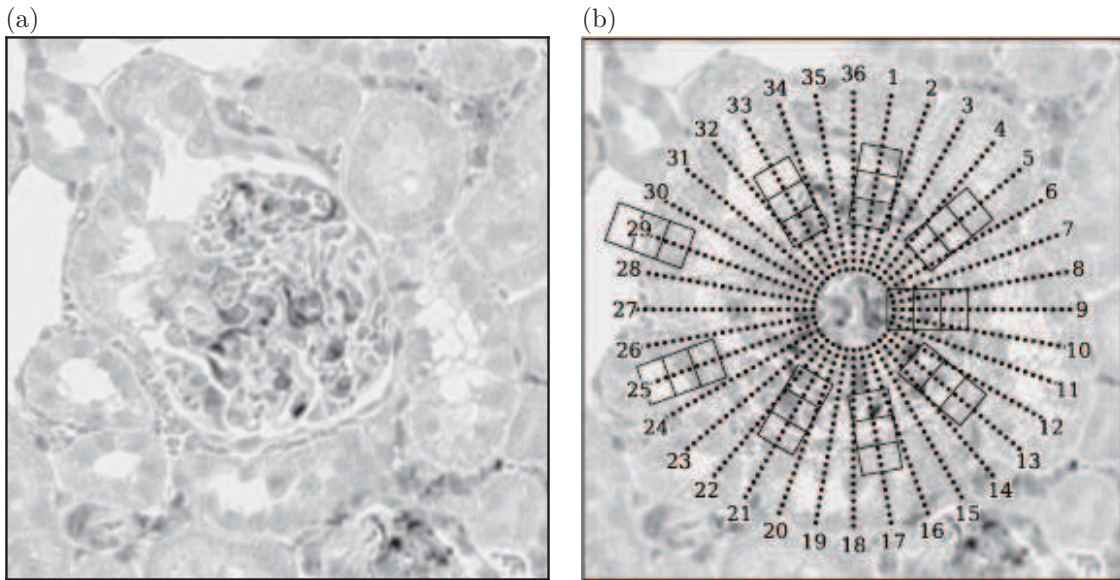


Figure 2: **Candidate Glomerulus and Line Segments.** S-HOG is based on the boundary of the objects of interest. Suppose the boundary of a candidate glomerulus (Panel(a)) is to be located. Boundary likeliness is computed at every point on $m(= 36)$ line segments placed uniformly in all m directions (Panel(b)). The boundary likeliness is computed at n points on each line segment. The n locations are depicted with dots in Panel (b).

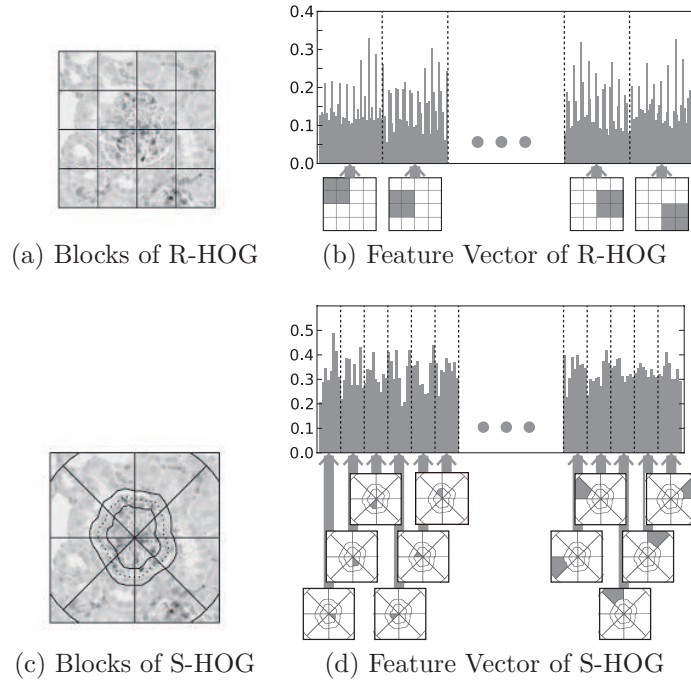


Figure 3: **Rectangular HOG and Segmental HOG.** R-HOG has been used for object detection in a wide variety of applications. R-HOG is the concatenation of statistics in each block in a grid dividing a rectangular region. On the other hand, the blocks of the proposed descriptor, S-HOG, are based on the segmentation of the object of interest.

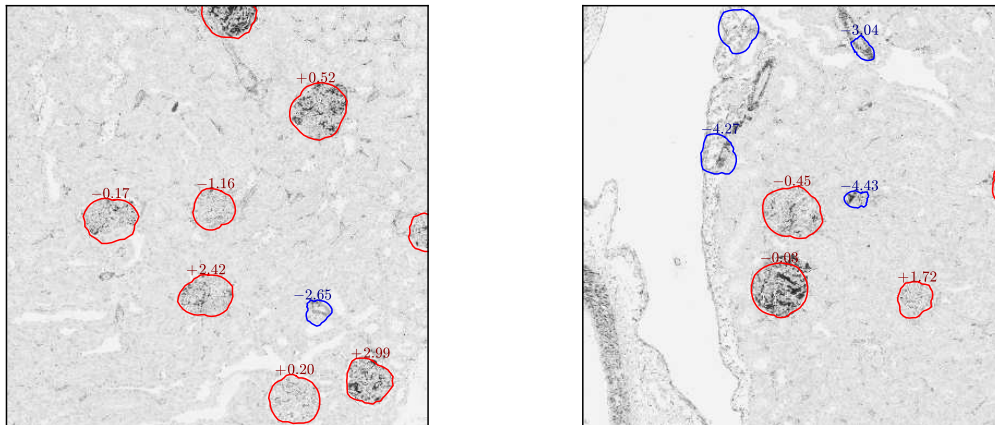


Figure 4: **Examples of Detected Glomeruli.** The estimated boundaries of the glomeruli are depicted with red rings. The areas surrounded with blue rings are passed through the pre-screening stage, but removed in the classification stage. The numbers are the SVM scores resulting from the classification stage. The areas with SVM scores over $\theta = -1.5$ are classified as a glomerulus. It can be observed that false positives such as vessels detected in the pre-screening stage were successfully removed in the classification stage.

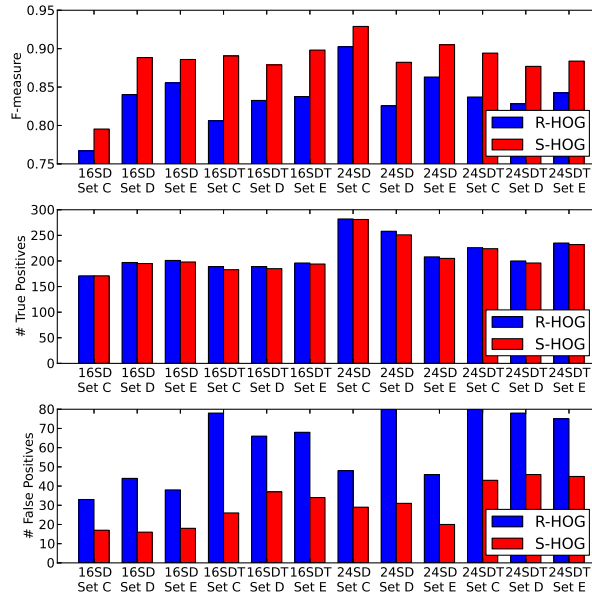


Figure 5: **Detection Performances.** The proposed descriptor, S-HOG, achieves evident improvement in F-measure compared to the existing descriptor, R-HOG. With small loss of true positives, S-HOG halves false positives of R-HOG. (See subsection on Detection Performance for details.)

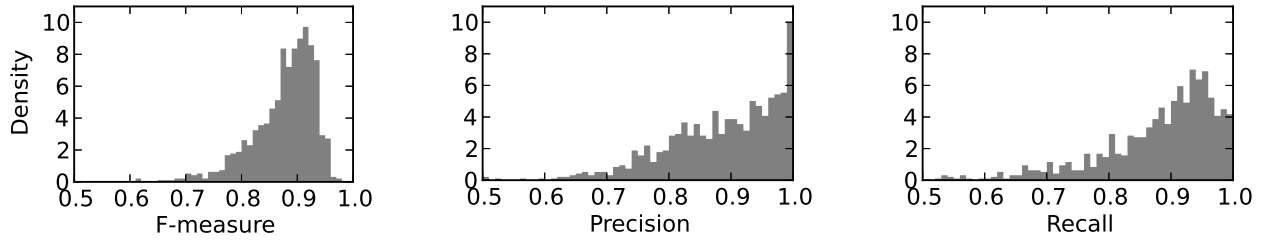


Figure 6: **Segmentation Performances.** The number of glomeruli are tallied to make a histogram with the F-measure, Precision, and Recall of the pixels based on comparison of true segmentation with estimated segmentation on the x -axes. (See Segmentation Performance subsection for details.)

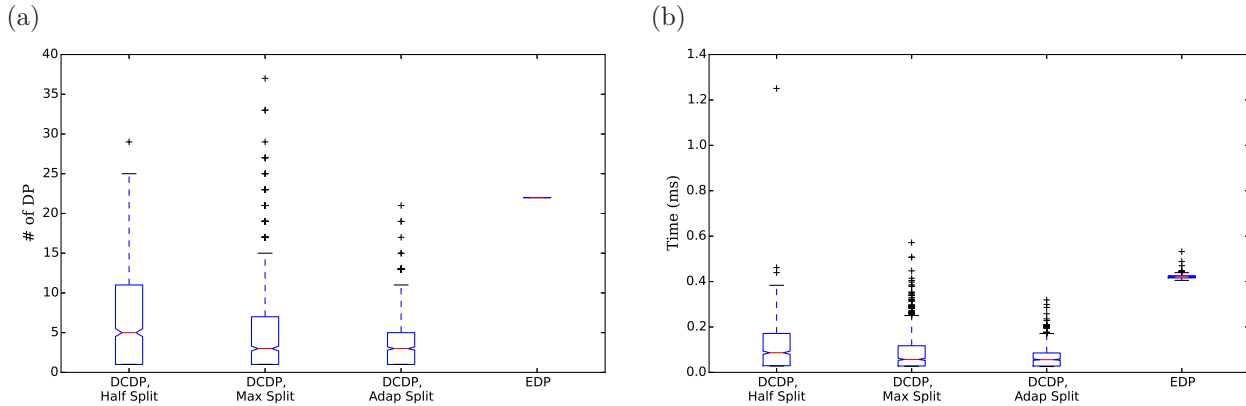


Figure 7: **Runtime Comparisons.** In Panel(a), n_{dp} of DCDP with three splitting schemes and EDP is shown, where n_{dp} is the number of invoking the $O(mn\varsigma)$ DP routine. The computational time of each algorithm is plotted in Panel(b).

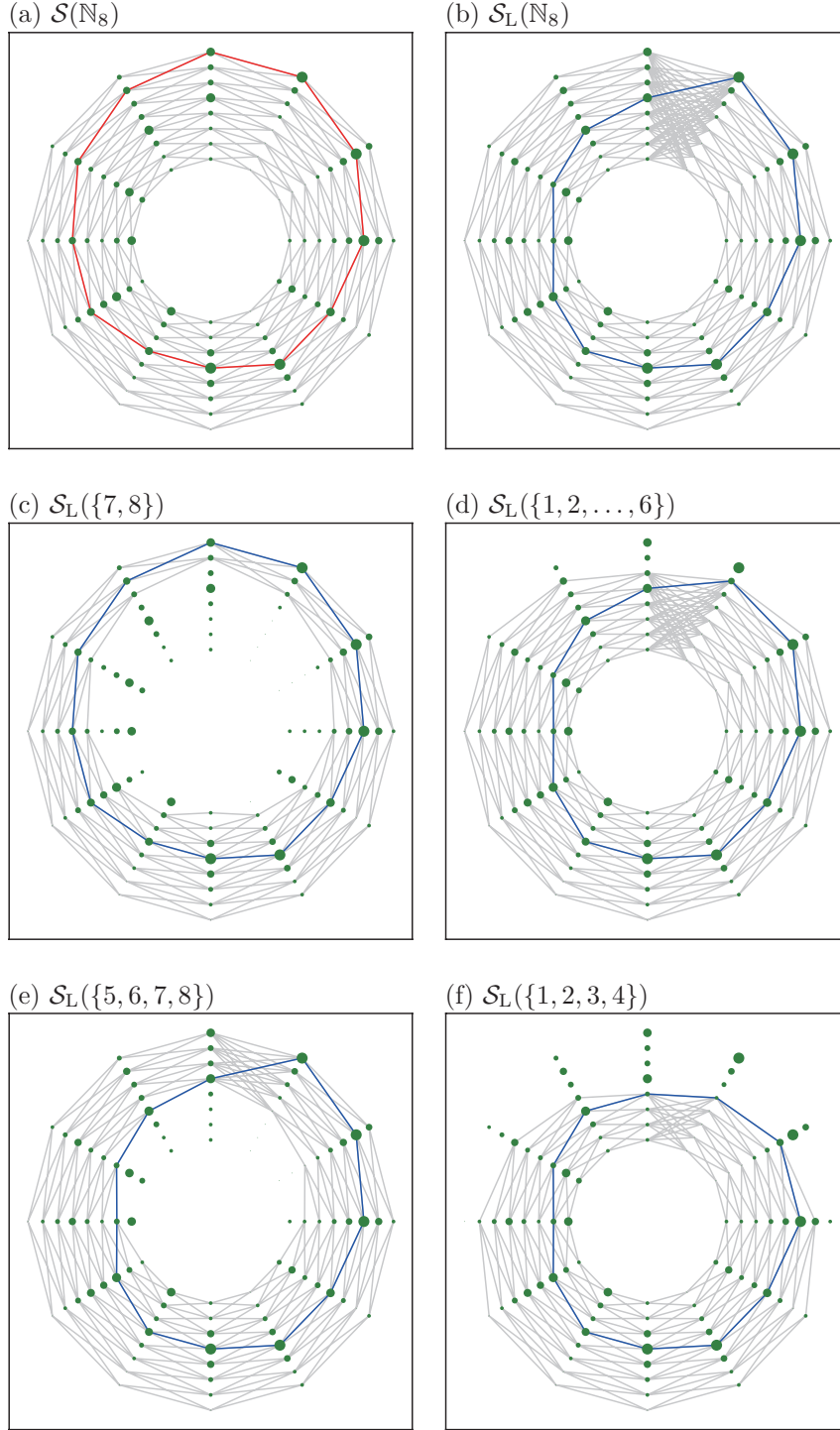


Figure 8: **Relaxed Problems in DCDP.** Here a segmentation problem (1) with $(n, m, \varsigma) = (12, 8, 1)$ is considered. In Panel (a), the sizes of red circles indicate the quantities of boundary likeliness. The feasible region $\mathcal{S}(\mathcal{I}_0)$ is the set of polygons, where $\mathcal{I}_0 = \mathbb{N}_n$. Overlapping all the polygons yields the gray edges. The optimal polygon is drawn with the red edges. DCDP relaxes the feasible region to get $\mathcal{S}_L(\mathcal{I}_0)$. In Panel (b), the relaxed feasible region $\mathcal{S}_L(\mathcal{I}_0)$ is depicted. The blue polygon is the optimal solution for the relaxed problem $\mathbf{p}_{L,0} = \operatorname{argmax}_{\mathbf{p} \in \mathcal{S}_L(\mathcal{I}_0)} J(\mathbf{p})$. The relaxed problems of four sub-problems with $\mathcal{S}_L(\{7, 8\})$, $\mathcal{S}_L(\{1, 2, \dots, 6\})$, $\mathcal{S}_L(\{5, 6, 7, 8\})$, and $\mathcal{S}_L(\{1, 2, 3, 4\})$ are illustrated in Panels (c),(d),(e),(f). The blue polygons in (c),(d),(e),(f) are the optimal solution of the four relaxed problems, respectively.